Applied and Computational Mechanics 18 (2024) 5–24

Wave dispersion analysis and evaluation of dynamic stress intensity factors using peridynamics approach

O. Bouaraquia[a], Y. Rafiq[a], M. Mabssout[a,*]

[a] *Laboratory of Mechanics and Civil Engineering, Faculty of Science and Technology, Tanger, Morocco*

Received 17 February 2024; accepted 6 June 2024

Abstract

The objective of this paper is to evaluate the dynamic stress intensity factors (DSIFs) of a cracked body using the bond-based peridynamics (BBPD) formulation. The peridynamics theory offers advantages over the classical continuum theory for solving partial differential equations in fracture mechanics. Nevertheless, some problems remain, such as its dispersion characteristics and constant micromodulus used in the classical BBPD. In this study, a Gaussian function is used to define the non-constant micromodulus. A wave dispersion analysis for a 1D problem was carried out and the influence of the horizon, mesh size and the kernel function on the dispersion properties were analyzed. On the other hand, a new approach to evaluate the DSIFs of a cracked body using the BBPD coupled with the displacement extrapolation technique is presented. Parameters that reduced the wave dispersion were kept for the DSIFs estimation. The proposed method is applied to analyze some benchmark examples. The obtained results are compared with the exact ones and they showed that the proposed approach can be used as an alternative method to evaluate DSIFs.

Keywords: bond-based peridynamics, wave dispersion, fracture mechanics, dynamic stress intensity factors, displacement extrapolation

1. Introduction

Understanding the behavior of a cracked structure under dynamic loading is very important in many engineering problems. Dynamic stress intensity factors (DSIFs) are one of the most important parameters in the analysis of dynamic fracture mechanics. Determination of this parameter is fundamental to check if the crack is stable or not. Some analytical methods have been introduced to compute the DSIFs. Nevertheless, the exact solution can be used only for a simple geometry. Therefore, in the past, several numerical methods have been developed for the evaluation of DSIFs. The most popular one is the finite element method [25], the boundary element method [6] and the extended finite element method [3].

However, mesh-based methods have faced challenges, particularly when dealing with large deformations or discontinuities. To overcome these difficulties, numerous meshfree methods have been developed for fracture simulation in cracked solids, such as the smoothed particle hydrodynamics [9], reproducing kernel particle method [16] and the element-free Galerkin method [4]. Nevertheless, all the numerical methods cited above are based on the local partial differential equations obtained from the classical continuum mechanics (CCM). However, for problems involving discontinuities, spatial derivatives of the displacements are undefined. To extend the classical formulation of CCM to problems with discontinuities, Silling introduced

*Corresponding author. Tel.: +212 539 393 954, e-mail: mmabssout@uae.ac.ma.
https://doi.org/10.24132/acm.2024.888

in [23] the peridynamics theory to model discontinuities without using the spatial derivatives. The peridynamics theory is a nonlocal extension of CCM for problems involving discontinuities or other singularities. In peridynamics, the spatial derivatives of the stress tensor in the equation of motion deduced from CCM are replaced with a nonlocal integral operator that does not require any spatial differentiability. This integral is based on the interaction between the material point and neighboring points inside a compact domain defined by its length scale called "horizon". The theoretical basis and numerical implementation of the peridynamics equations are presented in [17]. In [11], peridynamics has been successfully applied for modeling crack growth and crack branching in brittle materials. Recently for the treatment of wave propagation in unbounded domains, Dirichlet absorbing boundary conditions have been developed for BBPD in 2D elastic [21] and viscous [12] materials.

However, the nonlocal characteristics of peridynamics result in a dispersive dynamic response of the medium [2]. Thus, the propagation of elastic waves can undergo distortions and variations in the speed of harmonics which can lead to unreal crack behavior of solids under impact loading. Therefore, the wave dispersion problem should be addressed before applying the peridynamics to a dynamic fracture.

Wave dispersion in peridynamics has been investigated over the past decades and techniques have been proposed to reduce the dispersion phenomena [10]. The dispersion of the numerical scheme depends on the choice of the peridynamics parameters. To take into account the effect of the distance between particles in the horizon, different kernel functions have been proposed and used for BBPD formulation [15]. An appropriate choice of the kernel function can reduce the wave dispersion.

In this paper, a Gaussian function is used as a kernel function to define the non-constant micromodulus in the BBPD formulation. Dispersion properties in a 1D wave propagation will be investigated. We derive the dispersion relation and we analyze the effect of horizon size, mesh size and the effect of weighted function on the dispersion properties. We propose to minimize wave dispersion in elastic solids by choosing a combination of the shape of the kernel function, the size of the horizon and the particles density, so that the peridynamics solution approaches the classical continuum (non-dispersive) solution. In case of heterogeneous materials, the peridynamics model parameters must be calibrated using the experimental dispersion curve in order to minimize numerical dispersion [22].

On the other hand, the evaluation of dynamic stress intensity factors is important in analyzing fracture problems. Many techniques based on the peridynamics theory have been introduced to estimate static and dynamic stress intensity factors. In [13], Hu et al. developed an algorithm to compute the nonlocal J-integral in the BBPD model. Panchadhara et al. [18] estimated the stress intensity factors using peridynamics and they analyze the effect of loading rate on fracture initiation and propagation. In [26], Zhu and Oterkus estimated the stress intensity factors using displacement extrapolation method and the BBPD approach.

The objective of this paper is (i) to analyze the wave dispersion problem using the Gaussian kernel function. The dispersion relation is derived and the effects of the horizon size, material point size, and kernel functions on the dispersion properties are discussed; (ii) to propose an efficient algorithm to estimate DSIFs using the displacement extrapolation method combined with the BBPD theory. The spatial discretization is carried out using the particle-based meshfree method [24]. After computing the displacement field, DSIFs are evaluated using the displacement extrapolation method. To show the performance and the accuracy of the proposed approach, some examples are analyzed.

This paper is organized as follows. An overview of the BBPD theory is given in Section 2.

Numerical discretization of the governing equations is presented in Section 3. Dispersion analysis is performed in Section 4. In Section 5, extrapolation displacement technique for estimating DSIFs and numerical examples is presented. Conclusions are summarized in Section 6.

2. Overview of the BBPD model

The peridynamics theory, introduced by Silling in [23], is based on a nonlocal interaction concept where pairs of particles exchange internal forces within a specific radius δ called "horizon". In BBPD, the governing equation at the particle $\boldsymbol{x}$ is expressed by

$$\varrho\ddot{\boldsymbol{u}}(\boldsymbol{x},t) = \int_{\mathcal{H}_x} \boldsymbol{f}\Big(\boldsymbol{x}' - \boldsymbol{x}, \boldsymbol{u}(\boldsymbol{x}',t) - \boldsymbol{u}(\boldsymbol{x},t)\Big)\,\mathrm{d}V_{x'} + \boldsymbol{b}(\boldsymbol{x},t)\,, \tag{1}$$

where ϱ is the density, $\boldsymbol{u}(\boldsymbol{x},t)$ is the displacement at point $\boldsymbol{x}$ and time t, $\ddot{\boldsymbol{u}}(\boldsymbol{x},t)$ is the acceleration, $\boldsymbol{f}$ is the pairwise force density function, $\boldsymbol{b}$ is the body force, and $\mathcal{H}_x$ is the neighborhood of $\boldsymbol{x}$ defined by

$$\mathcal{H}_x = \{\boldsymbol{x}' \in \Omega : \|\boldsymbol{x}' - \boldsymbol{x}\| \leq \delta\}\,, \tag{2}$$

where δ is the horizon, i.e., the radius of the compact domain $\mathcal{H}_x$.

As shown in Fig. 1, the relative position $\boldsymbol{\xi}$ between two particles $\boldsymbol{x}$ and $\boldsymbol{x}'$ in the reference configuration and the relative displacement $\boldsymbol{\eta}$ in the deformed configuration are as follows

$$\boldsymbol{\xi} = \boldsymbol{x}' - \boldsymbol{x}, \qquad \boldsymbol{\eta} = \boldsymbol{u}(\boldsymbol{x}',t) - \boldsymbol{u}(\boldsymbol{x},t) \tag{3}$$

and $\boldsymbol{\xi} + \boldsymbol{\eta}$ is the current relative position vector between the particles. For a linear microelastic material, the BBPD function $\boldsymbol{f}$ can be expressed as [23]

$$\boldsymbol{f}(\boldsymbol{\xi},\boldsymbol{\eta}) = \frac{\partial w(\boldsymbol{\xi},\boldsymbol{\eta})}{\partial \boldsymbol{\eta}}\,, \tag{4}$$

where the micropotential function w is defined as [23, 24]

$$w(\boldsymbol{\xi},\boldsymbol{\eta}) = \frac{1}{2}\,c(\xi,\delta)s^2\xi\,, \tag{5}$$

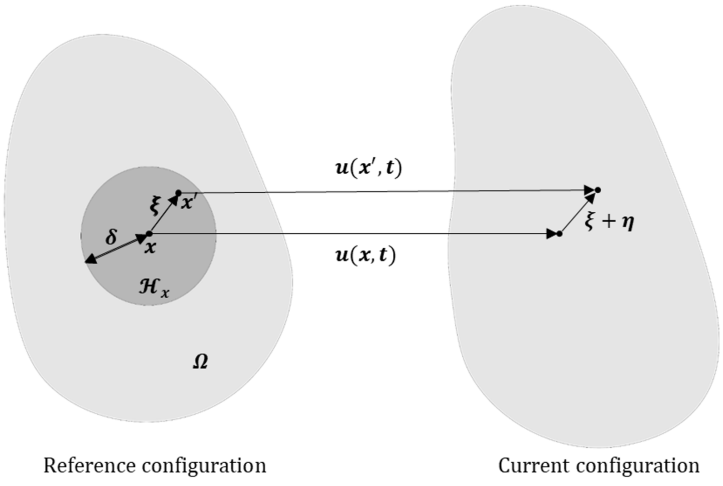

Fig. 1. Reference and current configurations of BBPD

where $\xi = \|\boldsymbol{\xi}\|$ is the magnitude of the bond in its initial configuration, $c(\xi, \delta)$ is the micromodulus function which represents the bond stiffness, and s is the relative elongation of a peridynamics bond defined as

$$s = \frac{\|\boldsymbol{\xi} + \boldsymbol{\eta}\| - \|\boldsymbol{\xi}\|}{\|\boldsymbol{\xi}\|} \,. \tag{6}$$

Equations (4) and (5) lead to the pairwise force function $\boldsymbol{f}$

$$\begin{aligned} \boldsymbol{f}(\boldsymbol{\xi}, \boldsymbol{\eta}) &= c(\xi, \delta) s \, \frac{\boldsymbol{\xi} + \boldsymbol{\eta}}{\|\boldsymbol{\xi} + \boldsymbol{\eta}\|} \qquad \text{for } \xi \leq \delta \,, \\ \boldsymbol{f}(\boldsymbol{\xi}, \boldsymbol{\eta}) &= 0 \qquad\qquad\qquad\quad \text{for } \xi > \delta \,, \end{aligned} \tag{7}$$

where $\|\boldsymbol{\xi} + \boldsymbol{\eta}\|$ is the magnitude of the bond in its deformed configuration.

To take into account the effect of the distance between particles on the stiffness of the bond, a kernel function is introduced in the expression of the micromodulus function

$$c(\boldsymbol{\xi}, \delta) = c_o(\delta) \, \overline{W}(\boldsymbol{\xi}, \delta) \,, \tag{8}$$

where $c_o(\delta)$ is the stiffness of the bond and $\overline{W}(\boldsymbol{\xi}, \delta)$ is the kernel function. In the classical BBPD, the kernel function is given by

$$\overline{W}(\boldsymbol{\xi}, \delta) = \begin{cases} 1 & \text{for } \xi \leq \delta, \\ 0 & \text{for } \xi > \delta. \end{cases} \tag{9}$$

This kernel function assumes equal contributions from all the material points in $\mathcal{H}_x$ and the internal length effect is ignored. To take into account the effect of the distance between particles, the following p-dependent kernel function is used:

$$\overline{W}(\xi, \delta) = \begin{cases} e^{-\left(\frac{p\xi}{\delta}\right)^2} & \text{for } \xi \leq \delta, \\ 0 & \text{for } \xi > \delta, \end{cases} \tag{10}$$

where p is an integer. The micromodulus $c_o(\delta)$ can be determined by equating the strain energy density obtained from BBPD with the strain energy density based on CCM at the material point $\boldsymbol{x}$

$$V^{\text{PD}}(\boldsymbol{x}) = V^{\text{CCM}}(\boldsymbol{x}) \,. \tag{11}$$

In a 2D plane stress problem, the strain energy density based on CCM is expressed as

$$V^{\text{CCM}}(\boldsymbol{x}) = \frac{1}{2} \, \boldsymbol{\varepsilon}^T \boldsymbol{D} \boldsymbol{\varepsilon} \,, \tag{12}$$

where the strain vector $\boldsymbol{\varepsilon}$ and the plane stress elastic matrix $\boldsymbol{D}$ are given by

$$\boldsymbol{\varepsilon} = \begin{bmatrix} \varepsilon_{11} \\ \varepsilon_{22} \\ 2\varepsilon_{12} \end{bmatrix} \qquad \text{and} \qquad \boldsymbol{D} = \frac{E}{1-\nu^2} \begin{bmatrix} 1 & \nu & 0 \\ \nu & 1 & 0 \\ 0 & 0 & \frac{1-\nu}{2} \end{bmatrix} , \tag{13}$$

where E is the Young's modulus and ν is the Poisson's ratio. Substituting (13) into (12), we obtain the expression for the strain energy density

$$V^{\text{CCM}}(\boldsymbol{x}) = \frac{E}{2\,(1-\nu^2)} \Big[\varepsilon_{11}^2 + \varepsilon_{22}^2 + 2\nu\varepsilon_{11}\varepsilon_{22} + 2(1-\nu)\varepsilon_{12}^2 \Big] . \tag{14}$$

In BBPD, the strain energy density at point $\boldsymbol{x}$ can be calculated as

$$V^{\text{PD}}(\boldsymbol{x}) = \frac{1}{2}\int\limits_{\mathcal{H}_x} w(\xi,\eta)\,\mathrm{d}V_x = \frac{1}{2}\int\limits_{\mathcal{H}_x} \frac{cs^2}{2}\xi\,\mathrm{d}V_x\,. \tag{15}$$

The bond stretch s is given by the normal strain component in the $\boldsymbol{n}$ direction

$$s = \varepsilon_n = \boldsymbol{n}^T\boldsymbol{\varepsilon}\boldsymbol{n}\,, \tag{16}$$

where $\boldsymbol{\varepsilon}$ is the strain tensor in 2D plane stress and $\boldsymbol{n}$ is the unit vector given by

$$\boldsymbol{n} = \cos\theta\boldsymbol{e}_1 + \sin\theta\boldsymbol{e}_2\,, \tag{17}$$

where $(\boldsymbol{e}_1, \boldsymbol{e}_2)$ are the unit vectors of the coordinate system in the initial configuration and θ is the angle between the normal $\boldsymbol{n}$ and the unit vector $\boldsymbol{e}_1$. Taking into account (8), (16) and (17), the strain energy density (15) is written as

$$V^{\text{PD}}(\boldsymbol{x}) = \frac{1}{4}\,h\int\limits_0^{\delta}\int\limits_0^{2\pi} c_0(\delta)\overline{W}(\xi,\delta)\varepsilon_n^2\xi^2\,\mathrm{d}\theta\,\mathrm{d}\xi\,, \tag{18}$$

where h is the unit thickness of the material.

In the following, we determine the micromodulus function for both the constant and Gaussian kernels.

Constant kernel:
Using the constant kernel function, equation (18) becomes

$$V^{\text{PD}}(\boldsymbol{x}) = \frac{hc_o(\delta)\pi\delta^3}{48}\left(3\varepsilon_{11}^2 + 3\varepsilon_{22}^2 + 2\varepsilon_{11}\varepsilon_{22} + 4\varepsilon_{12}^2\right). \tag{19}$$

To determine $c_o(\delta)$, we consider two types of deformations:

(1) Isotropic tensile deformation ($\varepsilon_1 = \varepsilon_2 = \varepsilon_o$ and $\varepsilon_{12} = 0$): In this case, equations (14) and (19) yield

$$V^{\text{CCM}} = \frac{E}{1-\nu}\varepsilon_o^2\,, \qquad V^{\text{PD}} = \frac{hc_o(\delta)\pi\delta^3}{6}\varepsilon_o^2\,. \tag{20}$$

By writing $(20)_1$ equal to $(20)_2$, we obtain the bond stiffness function for the constant kernel

$$c_o(\delta) = \frac{6E}{(1-\nu)h\pi\delta^3}\,. \tag{21}$$

(2) Pure shear deformation ($\varepsilon_1 = \varepsilon_2 = 0$ and $\varepsilon_{12} = \varepsilon_o$): In this case, equations (14) and (19) become

$$V^{\text{CCM}} = \frac{E}{1+\nu}\varepsilon_o^2\,, \qquad V^{\text{PD}} = \frac{hc_o(\delta)\pi\delta^3}{12}\varepsilon_o^2\,. \tag{22}$$

By equalizing $(22)_1$ and $(22)_2$, we obtain the following expression for the bond stiffness:

$$c_o(\delta) = \frac{12E}{(1+\nu)h\pi\delta^3}\,. \tag{23}$$

Equations (21) and (23) lead to the fixed Poisson's ratio $\nu = 1/3$ for 2D plane stress problems. Therefore, the expression of the micromodulus function is written as

$$c_o(\delta) = \frac{9E}{h\pi\delta^3}\,. \tag{24}$$

In the case of plane strain analysis, a similar calculation results in a limited Poisson's ratio $\nu = 1/4$ when the constant kernel is used. The function $c_o(\delta)$ is expressed as

$$c_o(\delta) = \frac{48E}{5h\pi\delta^3}\,. \tag{25}$$

In a 1D problem, writing the strain energy density leads to the expression

$$c_o(\delta) = \frac{2E}{A\delta^2}\,. \tag{26}$$

Gaussian kernel:
Similarly, inserting the kernel function (10) into (18), we obtain the strain energy density

$$V^{\text{PD}}(\boldsymbol{x}) = \frac{1}{4}\,h \int_0^{\delta}\int_0^{2\pi} c_o(\delta) e^{-\left(\frac{p\xi}{\delta}\right)^2} \varepsilon_n^2 \xi^2 \,\mathrm{d}\theta\,\mathrm{d}\xi\,. \tag{27}$$

The integration by parts of (27) gives

$$V^{\text{PD}}(\boldsymbol{x}) = \frac{hc_o(\delta)\pi}{16}\left(\frac{\sqrt{\pi}\delta^3 \text{erf}(p)}{4p^3} - \frac{\delta^3 e^{-p^2}}{2p^2}\right)\left(3\varepsilon_{11}^2 + 3\varepsilon_{22}^2 + 2\varepsilon_{11}\varepsilon_{22} + 4\varepsilon_{12}^2\right). \tag{28}$$

Solving the equation $V^{\text{CCM}} = V^{\text{PD}}$ leads to the expression

$$c_o(\delta) = \frac{12E}{h\pi\delta^3}\frac{p^3}{\sqrt{\pi}\text{erf}(p) - 2pe^{-p^2}}\,, \tag{29}$$

where erf$(.)$ is an error function. With $p = 2$, equation (29) gives

$$c_o(\delta) = \frac{96e^4 E}{\left(e^4\sqrt{\pi}\text{erf}(2) - 4\right)h\pi\delta^3}\,. \tag{30}$$

Therefore, the micromodulus function $c(\xi, \delta)$ is written as

$$c(\xi,\delta) = c_o(\delta)\overline{W} = \frac{96e^4 E}{(e^4\sqrt{\pi}\text{erf}(2) - 4)h\pi\delta^3} e^{-(\frac{2\xi}{\delta})^2}. \tag{31}$$

For a 1D analysis, the strain energy density is given by

$$V^{\text{PD}} = \frac{A}{4}\int_{-\delta}^{\delta} cs^2|\xi| d\xi = \frac{Ac_o(\delta)s^2\delta^2}{4p^2}(1 - e^{-p^2})\,. \tag{32}$$

Setting (32) equal to $V^{\text{CCM}} = 1/2E\varepsilon_o^2$ with $\varepsilon_o = s$ leads to

$$c_o(\delta) = \frac{2E}{A\delta^2}\frac{p^2}{1 - e^{-p^2}}\,. \tag{33}$$

Therefore, the expression of $c(\xi, \delta)$ is given by

$$c(\xi,\delta) = c_o(\delta)\overline{W} = \frac{2E}{A\delta^2}\frac{p^2}{1 - e^{-p^2}} e^{-(\frac{p\xi}{\delta})^2}\,. \tag{34}$$

The normalized micromodulus function with different values of p is presented in Fig. 2. As we can observe, the interactions become more local with increasing the p value.

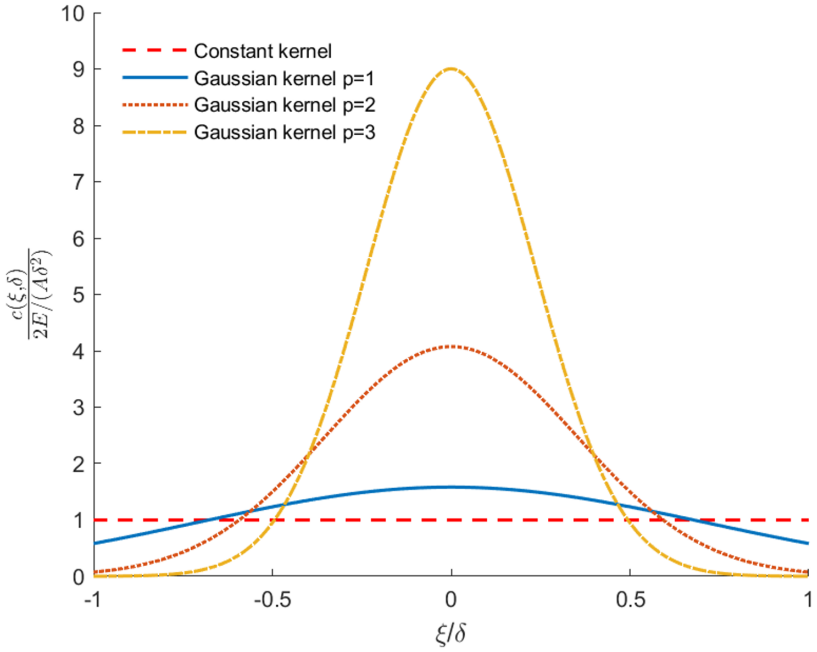

Fig. 2. Normalized micromodulus function for the constant and Gaussian kernel functions

3. Numerical model

3.1. Spatial discretization

Different methods can be used to discretize the peridynamics governing equation in space. The most common approach is the meshfree scheme [24]. Using this approach, the domain Ω is discretized with a number of nodes as shown in Fig. 3. In Ω, each node $\boldsymbol{x}_i \in \Omega$ is associated with a certain finite volume in the reference configuration, such that the set of nodes forms a uniform grid with grid spacing Δx, as shown in Fig. 3. For 2D problems, the volume associated with the node $\boldsymbol{x}_i$ is given by $V_j = \Delta x^2 h$, where h is the thickness of the domain.

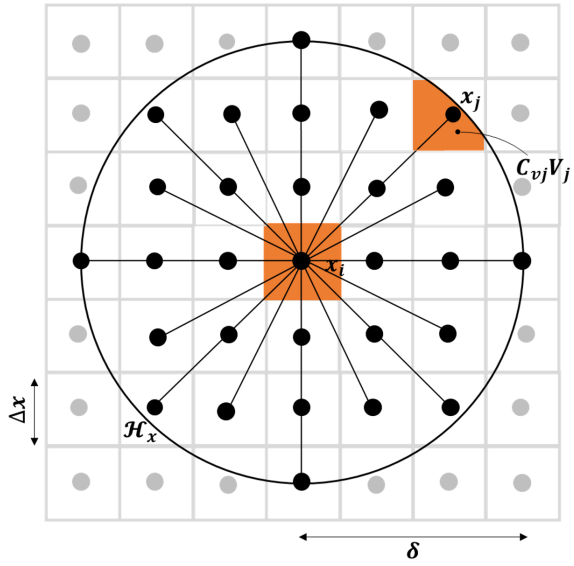

Fig. 3. Peridynamics 2D spatial discretization

The discretized form of the BBPD governing equation for any node $\boldsymbol{x}_i \in \Omega$ at time t_n is obtained by approximating the integral term in (1) into a summation over all the bonds within the horizon region using one Gauss point. The discretized motion equation is written as

$$\varrho \ddot{\boldsymbol{u}}_i^n = \sum_{j=1}^{N_{\mathcal{H}_x}} \boldsymbol{f}\Big(\boldsymbol{x_j} - \boldsymbol{x_i}\,,\boldsymbol{u}_j^n - \boldsymbol{u}_i^n\Big) C_{vj} V_j + \boldsymbol{b}_i^n\,, \tag{35}$$

where $N_{\mathcal{H}_x}$ is the total number of particles within the horizon region of the particle i, V_j is the volume of the j-th particle, and C_{vj} is the volume correction factor and it is used to approximate the portion of V_j covered by the neighborhood $\mathcal{H}_x$ (see Fig. 3) defined by [5]

$$C_{vj}(\xi) = \begin{cases} 1 & \text{for } \|\boldsymbol{\xi}\| \leq \delta - 0.5\Delta x, \\ \dfrac{\delta + 0.5\Delta x - \|\boldsymbol{\xi}\|}{\Delta x} & \text{for } \delta - 0.5\Delta x < \|\boldsymbol{\xi}\| < \delta + 0.5\Delta x, \\ 0 & \text{for } \|\boldsymbol{\xi}\| \geq \delta + 0.5\Delta x. \end{cases} \tag{36}$$

Equation (35) can be written as

$$\varrho \ddot{\boldsymbol{u}}_i^n = \sum_{j=1}^{N} \boldsymbol{f}_{ij}^n C_{vj} V_{\,j} + \boldsymbol{b}_i^n\,, \tag{37}$$

where the pairwise interaction force is given by

$$\boldsymbol{f}_{ij}^n = \boldsymbol{f}\left(\boldsymbol{\xi}_{ij}, \boldsymbol{\eta}_{ji}^n\right) = c s_{ij}^n \frac{\boldsymbol{\xi}_{ij} + \boldsymbol{\eta}_{ij}^n}{\left\|\boldsymbol{\xi}_{ij} + \boldsymbol{\eta}_{ij}^n\right\|}\,, \tag{38}$$

where $\boldsymbol{\xi}_{ij} = \boldsymbol{x}_j - \boldsymbol{x}_i$ and $\boldsymbol{\eta}_{ij}^n = \boldsymbol{u}_j^n - \boldsymbol{u}_i^n$ are the relative position and displacement, respectively. The stretch between two material points is written as

$$s_{ij}^n = \frac{\left\|\boldsymbol{\xi}_{ij} + \boldsymbol{\eta}_{ij}^{\boldsymbol{n}}\right\| - \|\boldsymbol{\xi}_{ij}\|}{\|\boldsymbol{\xi}_{ij}\|}\,. \tag{39}$$

3.2. Time discretization

The time integration of the semi discretized form (37) is performed using the central finite difference scheme. The acceleration at time $t^n = n\Delta t$ is approximated by

$$\ddot{\boldsymbol{u}}_i^n = \frac{\boldsymbol{u}_i^{n+1} - 2\boldsymbol{u}_i^n + \boldsymbol{u}_i^{n-1}}{\Delta t^2}\,. \tag{40}$$

Inserting (40) into (37) gives the displacement at time t^{n+1}

$$\boldsymbol{u}_i^{n+1} = \frac{\Delta t^2}{\varrho}\left[\sum_{j=1}^{N} \boldsymbol{f}_{ij}^n\, C_{vj} V_j + \boldsymbol{b}_i^n\right] + 2\boldsymbol{u}_i^n - \boldsymbol{u}_i^{n-1}\,. \tag{41}$$

Stability condition: Using the von Neumann stability analysis of (41) written in 1D, the following stability condition is obtained [24]:

$$\Delta t \leq \Delta t_{cr} = \sqrt{\frac{\varrho}{\sum_j V_j C_{ij}}}\,, \tag{42}$$

where V_j is the volume corresponding to the node j and C_{ij} is a scalar given by

$$C_{ij} = |C(\xi_{ij})| = \frac{c(\xi_{ij})}{|\xi_{ij}|}\,. \tag{43}$$

Note that the stability condition (42) is a necessary condition.

4. Wave dispersion analysis

4.1. Wave dispersion in a 1D bar

In this section, wave dispersion relation is derived for 1D BBPD. The effects of different parameters on the wave dispersion are investigated.

The constant and Gaussian kernels are used to analyze the numerical dispersion of a 1D elastic wave. Neglecting the body forces, the equation in 1D BBP is written as

$$\varrho\ddot{u}(x,t) = \int_{\mathcal{H}_x} c_o(\delta)\overline{W}(\xi,\delta)\frac{u'-u}{|x'-x|}\,\mathrm{d}x'\,. \tag{44}$$

To obtain the dispersion relation for an elastic media, it is sufficient to analyze one harmonic wave component which can be expressed as

$$u(x,t) = u_0 e^{i(kx-\omega t)}\,, \tag{45}$$

where u_o is the amplitude, i is the imaginary unit, k is the wave number, and ω is the angular frequency. Substituting (45) into (44) leads to the following dispersion relation:

$$\omega^2 = \int_{\mathcal{H}_x} \frac{c_o(\delta)\overline{W}(\xi,\delta)}{\varrho|\xi|}(1-\cos k\xi)\,\mathrm{d}x'\,. \tag{46}$$

In the discrete form, the horizon size δ and the relative position ξ are expressed in terms of the mesh spacing Δx as

$$\delta = m\Delta x\,, \qquad \xi = j\Delta x\,. \tag{47}$$

Therefore, the discretized form of (46) becomes

$$\omega^2 = \sum_{j\neq 0} \frac{c_o(m\Delta x)\overline{W}(j\Delta x, m\Delta x)}{\varrho|j|}(1-\cos jk\Delta x)\,. \tag{48}$$

For the constant kernel function, the dispersion relation $\omega(k)$ is as follows

$$\omega^2 = \frac{2v^2}{m^2\Delta x^2}\sum_{j\neq 0}\frac{1}{|j|}(1-\cos jk\Delta x)\,, \tag{49}$$

where the cross-sectional area A is taken equal to unity. When the Gaussian kernel is used, the dispersion relation is written as

$$\omega^2 = \frac{2v^2}{m^2\Delta x^2}\frac{p^2}{1-e^{-p^2}}\sum_{j\neq 0}\frac{1}{|j|}(1-\cos jk\Delta x)e^{-\left(p\frac{j}{m}\right)^2}\,, \tag{50}$$

where v is the classical wave speed given by $v=\sqrt{E/\varrho}$.

From (49) and (50), we observe that the dispersion of the elastic wave depends on the grid spacing, the number of material points inside the compact domain and the shape of the kernel function. Next, we analyze the variation of the normalized frequency $\widetilde{\omega}=\omega/v$ as a function of wavelength k for different values of m, Δx and p.

Figs. 4 and 5 show the dispersion curves $\widetilde{\omega}(k)$ using the Gaussian kernel function with $p=1$, $p=2$ and $m=3$. Different values of grid spacing Δx have been used. The increase

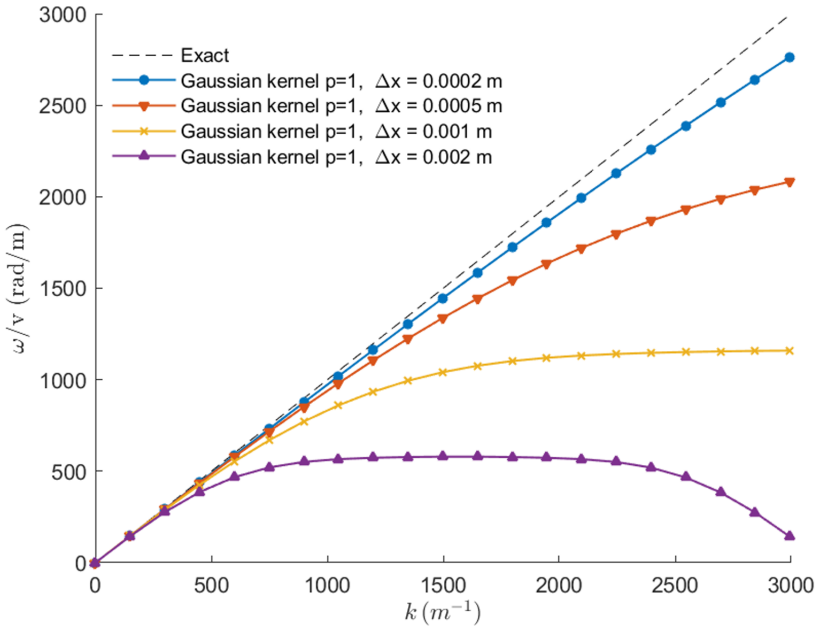

Fig. 4. Dispersion curves using the Gaussian kernel $(p = 1)$ for different grid spacing Δx

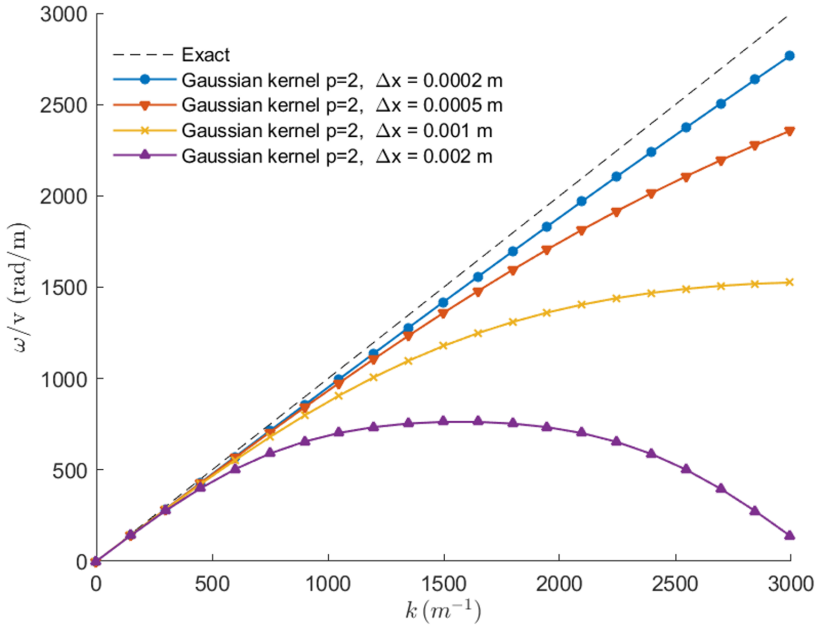

Fig. 5. Dispersion curves using the Gaussian kernel $(p = 2)$ for different grid spacing Δx

in Δx, i.e., the increase in $\delta = m\Delta x$, causes an increase in wave dispersion. For a large value of the wave number k, the dispersion significantly intensifies with the increasing grid spacing Δx. As Δx or $\delta \to 0$, the peridynamics numerical solution converges to the corresponding CCM solution (i.e., local theory). For comparison, the dispersion curve for the constant kernel function is plotted in Fig. 6. Using the constant kernel function, the interaction force between particle I and all the other particles J within its horizon is constant. However, when using the Gaussian kernel, the interaction forces decrease with an increase in the distance between the particles inside the horizon. Therefore, the wave dispersion is larger with the constant kernel

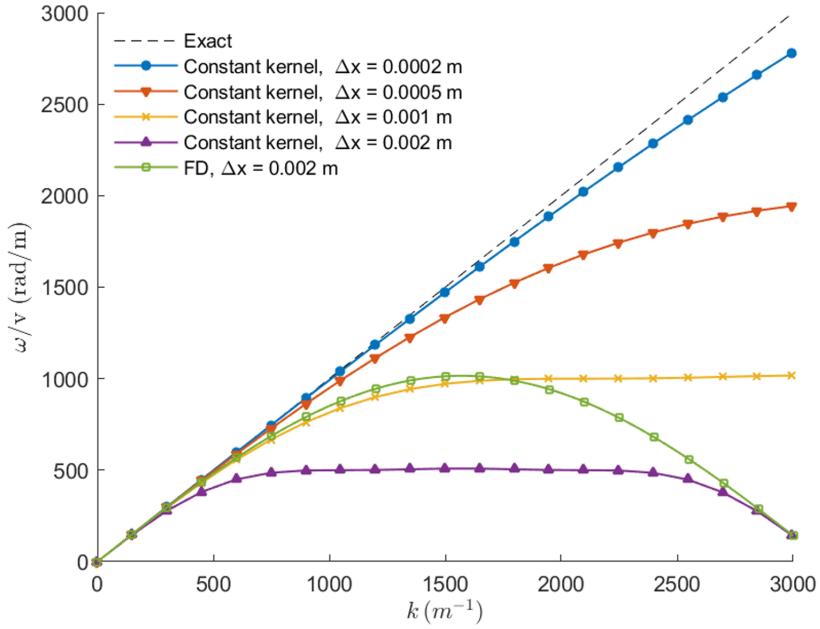

Fig. 6. Dispersion curves using the constant kernel for different grid spacing Δx (FD – finite difference dispersion curve)

than that obtained with the Gaussian kernel, as can be seen by comparing Figs. 4–6.

We observe that when $\Delta x = 0.002\,\mathrm{m}$, the dispersive curves $\widetilde{\omega}(k)$ diverge from the local dispersion curve for high wavenumbers, see Figs. 4–6. To clarify this point, we discretize the wave equation using the finite difference method. The dispersive relation for the central finite difference scheme is given by

$$\omega = \frac{2}{\Delta t} \sin^{-1}\left(C \, \sin \frac{k\Delta x}{2}\right), \tag{51}$$

where C is the Courant number given by

$$C = \frac{v \, \Delta t}{\Delta x} \, . \tag{52}$$

In Fig. 6, the finite difference (FD) dispersion curve is plotted with $\Delta x = 0.002\,\mathrm{m}$ and $C = 0.5$. As observed, both the dispersion curves for FD and peridynamics exhibit similar behavior for high wavenumbers. With the FD discretization, the shortest wavelength that can be represented on the mesh with spacing Δx is $\lambda_{\text{min}} = 2\Delta x$, which corresponds to the maximum wavenumber $k_{\text{max}} = \pi/\Delta x$. Values of k greater than k_{max} are irrelevant since these correspond to wavelength values whose waves are too short to be represented on a mesh with spacing Δx. Therefore, the peridynamics dispersion curve $\widetilde{\omega}(k, \Delta x = 0.002\,\mathrm{m})$ diverges from the local solution for $k > k_{\text{max}} = 1\,570.79\,\mathrm{m}^{-1}$ regardless of the kernel function used in the model.

Another interesting test involves the variation of the number of points in the horizon while keeping the horizon δ constant ($\delta = 4\,\mathrm{mm}$). The results are shown in Figs. 7, 8 and 9 for $p = 1, 2$ and the constant kernel, respectively. As $m = \delta/\Delta x$ increases, the peridynamics approximation converges to the nonlocal peridynamics solution, which can be highly dispersive depending on the size of the horizon δ. It is important to note that when increasing m and keeping δ constant, the method does not provide more accurate numerical solutions, as shown

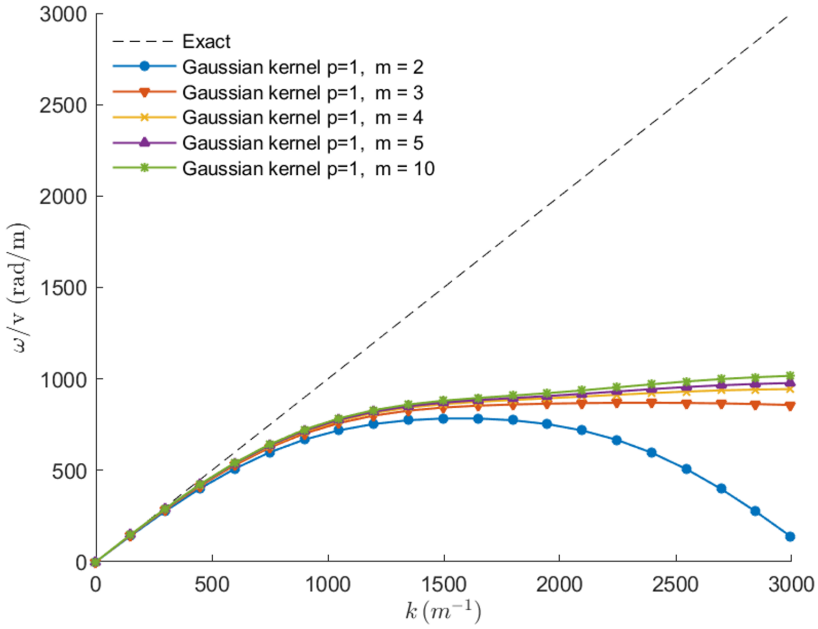

Fig. 7. Dispersion curves using the Gaussian kernel with $p = 1$ for various values of m

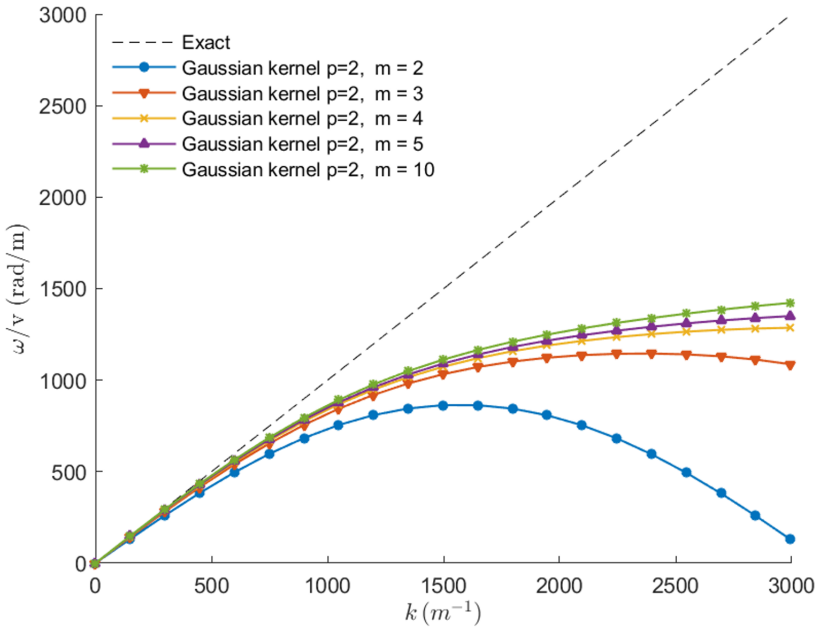

Fig. 8. Dispersion curves using the Gaussian kernel with $p = 2$ for various values of m

in Figs. 7–9. For $m = 2$, the solution deviates from the nonlocal peridynamics solution. This case corresponds to $\Delta x = 0.002$ m, and as mentioned above, the dispersion curve diverges from the local dispersion solution for $k > k_{\max} = 1\,570.79\,\mathrm{m}^{-1}$. Hence, a minimum value of $m = 3$ is required for convergence.

Finally, Fig. 10 shows a comparison of the dispersion curves for the constant kernel and the Gaussian kernel with $p = 1$ and $p = 2$. Parameters $m = 10$ and $\delta = 4$ mm are used in this analysis. As expected, we observe that as p increases, less dispersion appears.

In conclusion, when analyzing problems involving wave propagation, it is important that

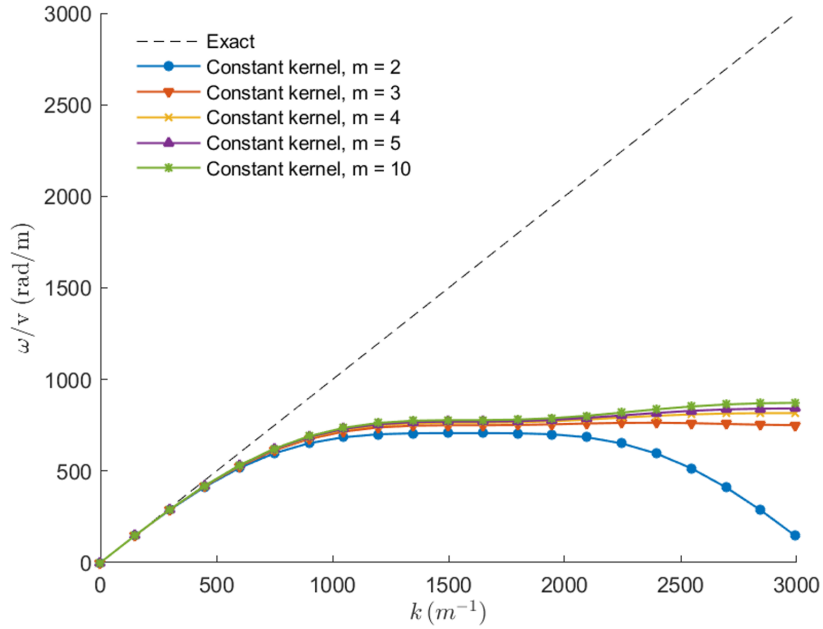

Fig. 9. Dispersion curves using the constant kernel for various values of m

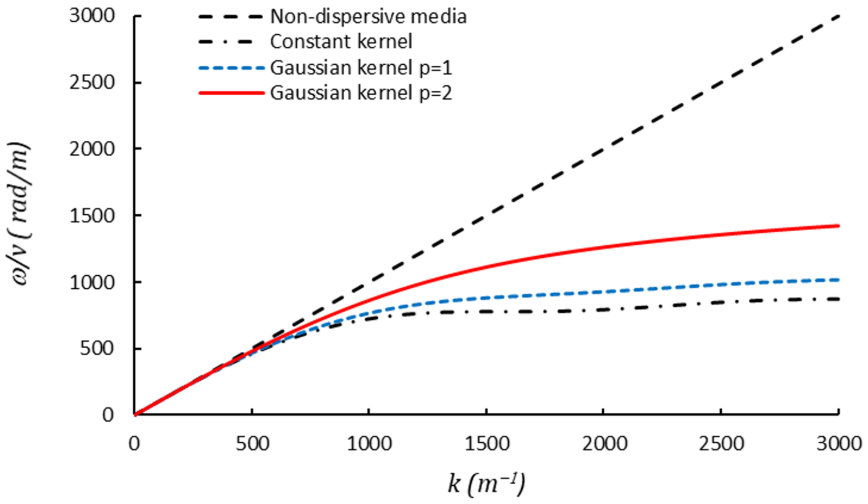

Fig. 10. Dispersion curves for different kernel functions

the horizon size, the material point size and the p-parameter should be chosen according to the dispersion curve.

4.2. Wave propagation in a 1D bar

In this section, we analyze the convergence of the peridynamics model to the classical solution of the 1D wave propagation problem using the constant and Gaussian kernel functions. Let us consider a uniform bar of length $L = 1\,\text{m}$, density $\varrho = 7\,850\,\text{kg}\,\text{m}^{-3}$, cross-sectional area $A = 1\,\text{mm}^2$ and elastic modulus $E = 200\,\text{GPa}$, fixed at the left end and free at the other one, as shown in Fig. 11. The bar is subjected to an intial force $F_o = 200\,\text{N}$. The boundary and initial conditions can be specified as follows:

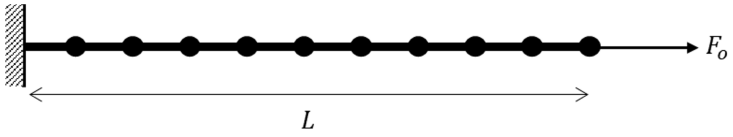

Fig. 11. Spatial discretization of the 1D bar subjected to an axial force

Boundary conditions

$$u(0,t)=0, \qquad \frac{\partial u}{\partial x}(L,t)=0. \tag{53}$$

Initial conditions

$$u(x,0)=\frac{F_o x}{EA}=10^{-3}x, \qquad \dot{u}(x,0)=0. \tag{54}$$

The peridynamics simulation is performed using the constant kernel and the Gaussian function with $p=2$, the grid spacing $\Delta x=1.25\,\text{mm}$ and the horizon size $\delta=m\Delta x=6.25\,\text{mm}$. The time step used in this analysis is $\Delta t=10^{-8}\,\text{s}$. The exact displacement solution of this problem is given by [19]

$$u(x,t)=\frac{8F_oL}{\pi^2AE}\sum_{n=0}^{\infty}\frac{(-1)^n}{(2n+1)^2}\sin\left(\frac{(2n+1)\pi x}{2L}\right)\cos\left(\frac{(2n+1)\pi ct}{2L}\right), \tag{55}$$

where $c=\sqrt{E/\varrho}$ is the classical wave speed. The exact strain is expressed as

$$\varepsilon(x,t)=\frac{4F_o}{\pi AE}\sum_{n=0}^{\infty}\frac{(-1)^n}{2n+1}\cos\left(\frac{(2n+1)\pi x}{2L}\right)\cos\left(\frac{(2n+1)\pi ct}{2L}\right). \tag{56}$$

Fig. 12 shows the strain time curves at $x=50\,\text{cm}$ calculated using the constant kernel and the Gaussian kernel with $p=2$. To verify the convergence of the numerical results based on the peridynamics, the exact strain history is also plotted. As we can observe, the numerical strains of the two cases converge to the exact solution. However, oscillations appear in the

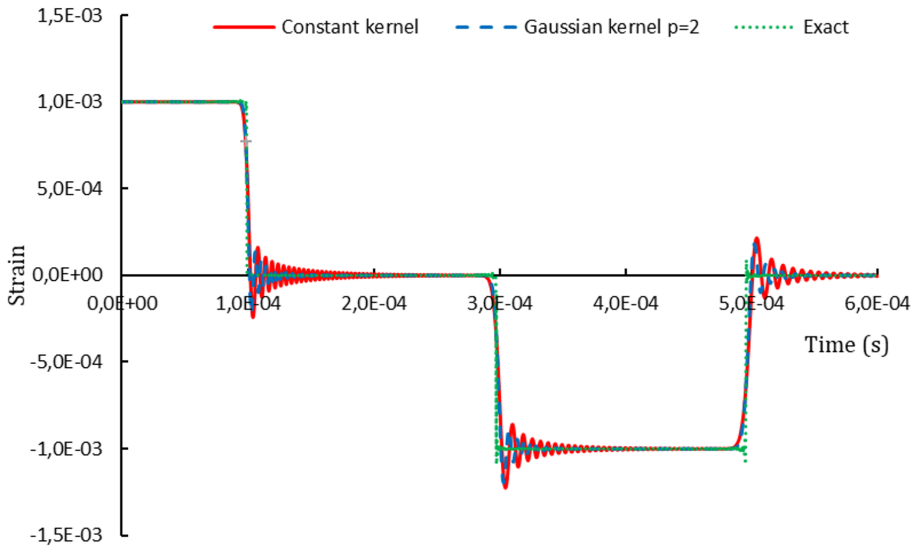

Fig. 12. Comparison between the exact solution and the BBPD results using the constant and Gaussian kernels

peridynamics simulation at the wave discontinuities. As expected, using the constant kernel, the oscillations are higher than those obtained with the Gaussian kernel.

5. Evaluation of DSIFs

5.1. Displacement extrapolation method

Different methods have been used for the evaluation of dynamic stress intensity factors (DSIFs), we can cite the path-independent J-integral [20] and the extrapolation method [1]. In this paper, the displacement extrapolation method is used to estimate DSIFs. The displacement field around the crack tip under Mode-I and Mode-II loading conditions for linear elastic materials is given by [8]

- *Mode-I:*

$$u_1 = \frac{K_I}{2\mu}\sqrt{\frac{r}{2\pi}}\cos\frac{\theta}{2}\left(\kappa - \cos\theta\right) , \quad u_2 = \frac{K_I}{2\mu}\sqrt{\frac{r}{2\pi}}\sin\frac{\theta}{2}\left(\kappa - \cos\theta\right) . \tag{57}$$

- *Mode-II :*

$$u_1 = \frac{K_{II}}{2\mu}\sqrt{\frac{r}{2\pi}}\sin\frac{\theta}{2}(2 + \kappa + \cos\theta) , \quad u_2 = \frac{K_{II}}{2\mu}\sqrt{\frac{r}{2\pi}}\cos\frac{\theta}{2}\left(2 - \kappa - \cos\theta\right) \tag{58}$$

with

$$\kappa = \begin{cases} 3 - 4\nu & \text{for plane strain,} \\ \dfrac{3-\nu}{1+\nu} & \text{for plane stress.} \end{cases} \tag{59}$$

From $(57)_2$ and $(58)_1$, expressions of DSIFs for the Mode-I and Mode-II are obtained

$$\left\{ \begin{array}{c} K_I \\ K_{II} \end{array} \right\} = \lim_{r\to 0} \frac{2\mu}{\kappa+1}\sqrt{\frac{2\pi}{r}} \left\{ \begin{array}{c} u_2(r,\pi) \\ u_1(r,\pi) \end{array} \right\} , \tag{60}$$

where r denotes the radial coordinate with the origin at the crack tip, μ is the shear modulus at the crack tip, and $u_1(r,\pi)$, $u_2(r,\pi)$ are the crack surface displacements computed using the BBPD model.

Along the crack surface near the crack tip, it can be assumed that

$$u_2(r)\, r^{-\frac{1}{2}} = A_1 + B_1 r, \tag{61}$$

where A_1 and B_1 are constants that can be determined using the displacements of points B, C, D, E as shown in Fig. 13. Therefore, the DSIFs for the Mode-I can be evaluated as

$$K_I(t) = \frac{2\mu\sqrt{2\pi}}{\kappa+1}\,\frac{u_2^B(t)\frac{r_2}{\sqrt{r_1}} - u_2^D(t)\frac{r_1}{\sqrt{r_2}}}{r_2 - r_1} \tag{62}$$

and the DSIFs for the Mode-II can be estimated as

$$K_{II}(t) = \frac{2\mu\sqrt{2\pi}}{\kappa+1}\,\frac{u_1^B(t)\frac{r_2}{\sqrt{r_1}} - u_1^D(t)\frac{r_1}{\sqrt{r_2}}}{r_2 - r_1} . \tag{63}$$

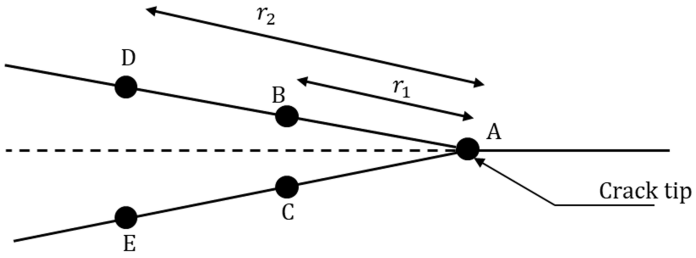

Fig. 13. Nodes close to the crack tip

5.2. Numerical examples

Two examples of the Mode-I and Mode-II loading are analyzed and DSIFs are estimated using the displacement extrapolation method coupled to the bond-based peridynamics. The Gaussian and the constant kernels are used in the BBPD approximation.

5.2.1. Stationary Mode-I semi-infinite crack

The displacement extrapolation method coupled to BBPD is used to compute DSIFs for a semi-infinite lateral crack in an infinite plate, as shown in Fig. 14. The Gaussian and constant kernels $\overline{W}(\boldsymbol{\xi}, \delta)$ are used in the computation under plane stress conditions. To assess the effectiveness of the proposed method in determining DSIFs, the numerical results are compared to the analytical solution published in [7].

The plate dimensions are: length $L = 10\,\text{m}$, height $2H = 4\,\text{m}$ and crack length $a = 5\,\text{m}$. The material properties are: Young's modulus $E = 210\,\text{GPa}$, Poisson's ratio $\nu = 0.3$ and density $\varrho = 8\,000\,\text{kg}\,\text{m}^{-3}$. The grid space $\Delta = 0.05\,\text{m}$ is used with a uniform distribution of material points and the total number of particles used is 200×80. A value of $\delta = 3\Delta$ was selected for the horizon. The time step used in the computation is $\Delta t = 5 \times 10^{-6}\,\text{s}$.

The ramp loading applied traction

$$\sigma(t) = \begin{cases} \sigma_0 \dfrac{t}{t_d} & \text{for } t \leq t_d, \\ \sigma_0 & \text{for } t \geq t_d, \end{cases} \tag{64}$$

where t_d is the rise time of the ramp load. In this example, $t_d = 3.36 \times 10^{-4}\,\text{s}$. For $t \leq t_c$, the

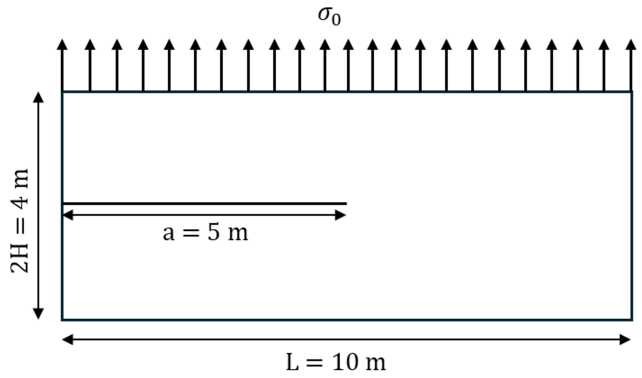

Fig. 14. Geometry and loading of the semi-infinite plate

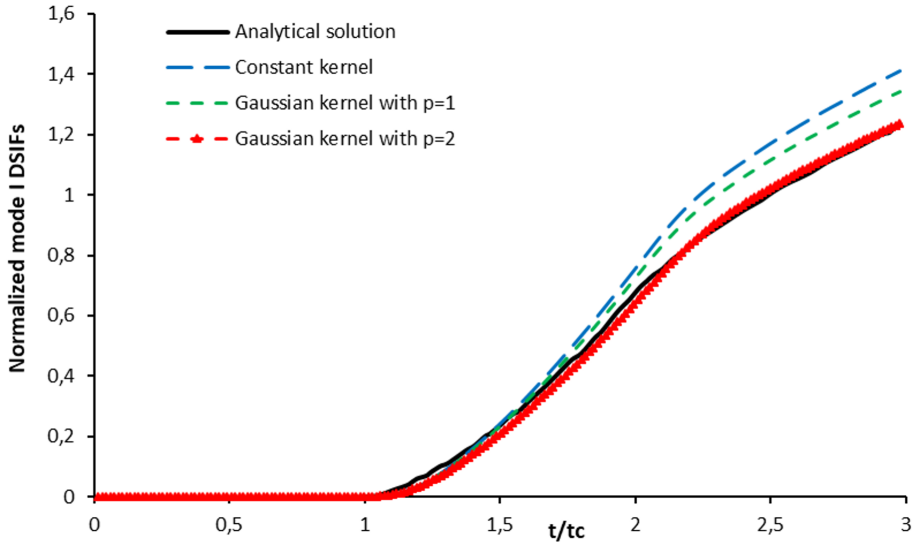

Fig. 15. Normalized Mode-I DSIFs for ramp loading with different kernel functions

analytical solution is given by [7]

$$K_I(\bar{t}) = \begin{cases} \dfrac{4}{3\pi}\dfrac{\sqrt{1-2\nu}}{1-\nu}\sigma_o\sqrt{\pi C_d t_d}\left(\dfrac{\bar{t}}{t_d}\right)^{\frac{3}{2}} & \text{for } 0 \le \bar{t} \le t_d, \\ \dfrac{4}{3\pi}\dfrac{\sqrt{1-2\nu}}{1-\nu}\sigma_o\sqrt{\pi C_d t_d}\left[\left(\dfrac{\bar{t}}{t_d}\right)^{\frac{3}{2}} - \left(\dfrac{\bar{t}}{t_d}-1\right)^{\frac{3}{2}}\right] & \text{for } \bar{t} \ge t_d, \end{cases} \tag{65}$$

where $\bar{t} = t - t_c$, $t_c = H/C_d$ is the time required for the stress wave to propagate to the tip of the crack, and C_d is the velocity for the longitudinal wave. The normalized DSIF is given by

$$\widetilde{K}_I(t) = \frac{K_I(t)}{\sigma_o\sqrt{H}}. \tag{66}$$

The normalized Mode-I DSIFs evaluated using (62) are shown in Fig. 15 for the constant and Gaussian kernel functions. The exact solution is also plotted for comparison. Displacements are determined using BBPD under plane stress conditions. As we can observe, there is an excellent agreement between the numerical results with kernel function $\overline{W}(\boldsymbol{\xi}, \delta, p = 2)$ and the analytical solution. For $\overline{W}(\boldsymbol{\xi}, \delta) = 1$, the numerical solution deviates from the exact solution. The same example is analyzed with the step loading function $\sigma(t) = \sigma_o H(t)$, where $H(t)$ is the Heaviside function. In this case, the exact solution is given [7]

$$K_I(t) = \begin{cases} 0 & \text{for } t < t_c, \\ \dfrac{2\sigma_0}{1-\nu}\sqrt{\dfrac{c_d}{\pi}(1-2\nu)\,(t-t_c)} & \text{for } t \ge t_c. \end{cases} \tag{67}$$

Fig. 16 plots the normalized Mode-I DSIFs for different kernel functions. Close to the time t_c, a deviation of the three curves from the exact solution is observed. This deviation is due to the discontinuity of the applied loading at $t = 0$. However, the Gaussian kernel function with $p = 2$ converges better to the analytical solution.

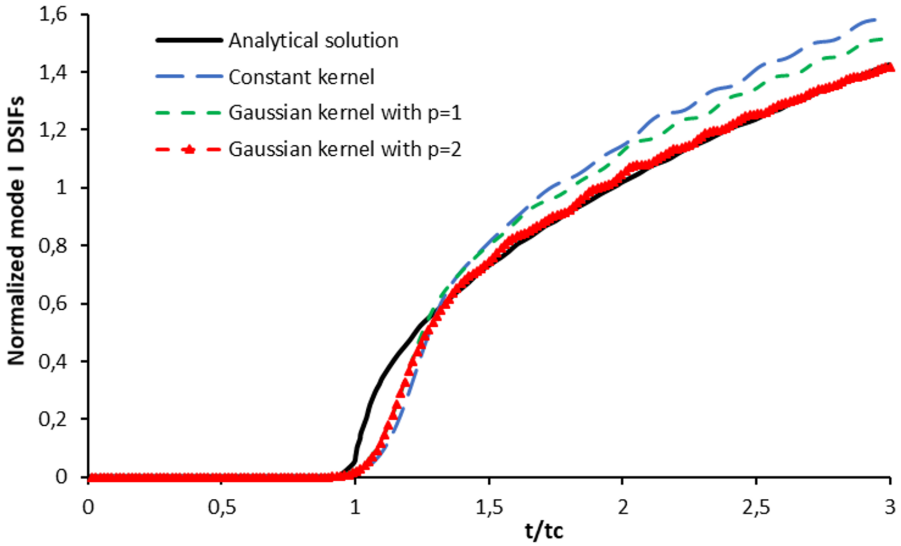

Fig. 16. Normalized Mode-I DSIFs for step loading with different kernel functions

5.2.2. Mode-II example

In this example, the proposed method is used to compute the Mode-II DSIFs of a cracked rectangular plate subjected to a uniform shear loading τ, as shown in Fig. 17.

The plate dimensions are: length $L = 104\,\text{mm}$, height $H = 40\,\text{mm}$ and the crack length $2a = 24\,\text{mm}$. The material properties are: Young's modulus $E = 73.5\,\text{GPa}$, Poisson's ratio $\nu = 0.25$ and density $\varrho = 2\,450\,\text{kg m}^{-3}$. The grid spacing used in this example is $\Delta = 0.26\,\text{mm}$ and the horizon $\delta = 3\Delta$. Fig. 18 shows the normalized Mode-II DSIFs $\widetilde{K}_{II}(t) = K_{II}(t)/(\tau\sqrt{\pi a})$ for the Gaussian and constant kernel functions. $K_{II}(t)$ are computed using the extrapolation technique (63) combined with BBPD. The results calculated using the J-integral [14] are also plotted. As we can observe, the Gaussian kernel with $p = 2$ shows a good agreement with the obtained results reported in [14].

6. Conclusions

In this paper, two points have been discussed utilizing the BBPD theory: the analysis of elastic wave dispersion in a 1D problem and the evaluation of dynamic stress intensity factors using displacement extrapolation. The results demonstrate that BBPD with the Gaussian kernel reduces the numerical dispersion compared to the classical BBPD model. Moreover, to show the

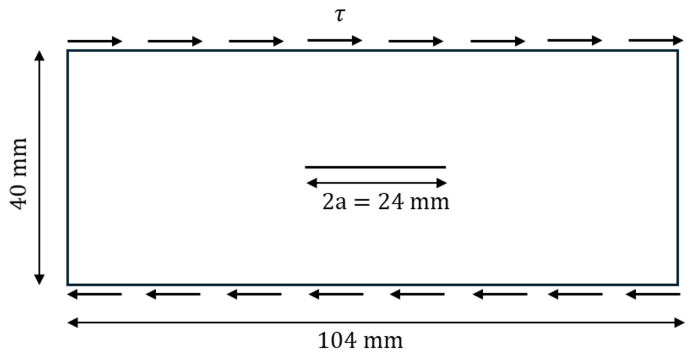

Fig. 17. Plate subjected to shear loading

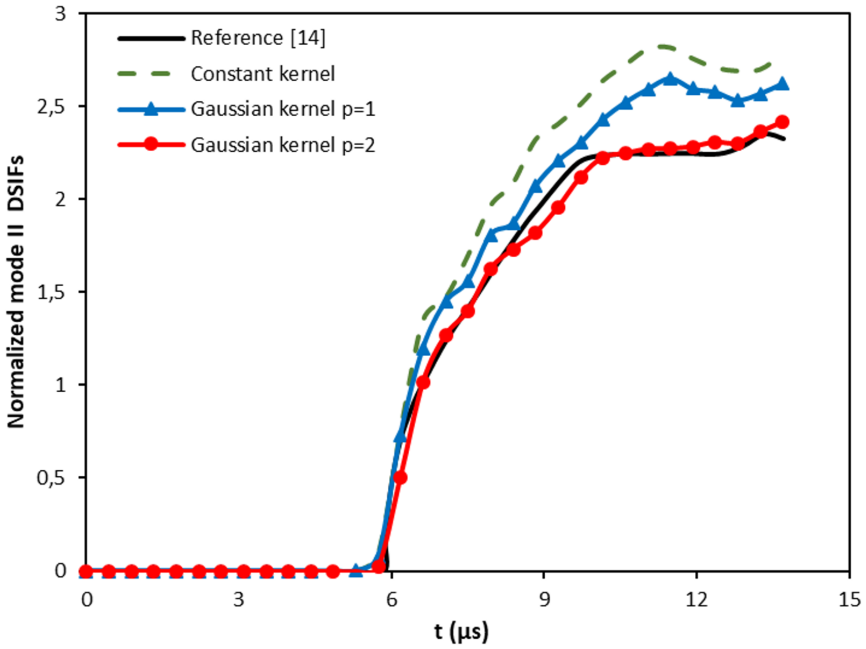

Fig. 18. Normalized Mode-II DSIFs for different kernel functions

performance of the proposed approach to estimate DSIFs, two examples of Mode-I and Mode-II are analyzed. A good agreement is observed between the numerical results obtained with the Gaussian kernel and the analytical and numerical results obtained by other numerical methods. Finally, the proposed approach can be used as an alternative technique for estimating dynamic stress intensity factors.

References

[1] Aliabadi, M. H., The boundary element method, Volume 2: Applications in solids and structures, John Wiley & Sons, 2002.

[2] Bažant, Z. P., Luo, W., Chau, V. T., Bessa, M. A., Wave dispersion and basic concepts of peridynamics compared to classical nonlocal damage models, Journal of Applied Mechanics 83 (11) (2016) No. 111004. https://doi.org/10.1115/1.4034319

[3] Belytschko, T., Black, T., Elastic crack growth in finite elements with minimal remeshing, International Journal for Numerical Methods in Engineering 45 (1999) 601–620. https://doi.org/10.1002/(SICI)1097-0207(19990620)45:5⟨601::AID-NME598⟩3.0.CO;2-S

[4] Belytschko, T., Lu, Y. Y., Gu, L., Crack propagation by element-free Galerkin methods, Engineering Fracture Mechanics 51 (2) (1995) 295–315. https://doi.org/10.1016/0013-7944(94)00153-9

[5] Bobaru, F., Foster, J. T., Geubelle, P. H., Silling, S. A., Handbook of peridynamic material, CRC Press, 2017. https://doi.org/10.1201/9781315373331

[6] Chirino, F., Dominguez, J., Dynamic analysis of cracks using boundary element method, Engineering Fracture Mechanics 34 (1989) 1051–1061. https://doi.org/10.1016/0013-7944(89)90266-X

[7] Freund, L. B., Dynamic fracture mechanics, Cambridge University Press, 1990. https://doi.org/10.1017/CBO9780511546761

[8] Gdoutos, E. E., Fracture mechanics, 2nd Edition, Springer, 2005.

[9] Gingold, R. A., Monaghan, J. J., Smoothed particle hydrodynamics: Theory and application to nonspherical star, Monthly Notices of the Royal Astronomical Society 181 (1977) 375–389. https://doi.org/10.1093/mnras/181.3.375

[10] Gu, X., Zhang, Q., Huang, D., Yv, Y., Wave dispersion analysis and simulation method for concrete SHPB test in peridynamics, Engineering Fracture Mechanics 160 (2016) 124–137. https://doi.org/10.1016/j.engfracmech.2016.04.005

[11] Ha, Y. D., Bobaru, F., Studies of dynamic crack propagation and crack branching with peridynamics, International Journal of Fracture 162 (2010) 229–244. https://doi.org/10.1007/s10704-010-9442-4

[12] Hermann, A., Shojaei, A., Seleson, P., Cyron, C. J., Silling, S. A., Dirichlet-type absorbing boundary conditions for peridynamic scalar waves in two-dimensional viscous media, International Journal for Numerical Methods in Engineering 124 (2023) 3 524–3 553. https://doi.org/10.1002/nme.7260

[13] Hu, W., Ha, Y. D., Bobaru, F., Silling, S. A., The formulation and computation of the nonlocal J-integral in bond-based peridynamics, International Journal of Fracture 176 (2012) 195–206. https://doi.org/10.1007/s10704-012-9745-8

[14] Kishimoto, K., Aoki, S., Sakata, M., Dynamic stress intensity factors using J-integral and finite element method, Engineering Fracture Mechanics 13 (2) (1980) 387–394. https://doi.org/10.1016/0013-7944(80)90067-3

[15] Li, S., Jin, Y., Lu, H., Sun, P., Huang, X., Chen, Z., Wave dispersion and quantitative accuracy analysis of bond-based peridynamic models with different attenuation functions, Computational Materials Science 197 (2021) No. 110667. https://doi.org/10.1016/j.commatsci.2021.110667

[16] Liu, W. K., Jun, S., Zhang, Y. F., Reproducing kernel particle methods, International Journal for Numerical Methods in Fluids 20 (8–9) (1995) 1081–1106. https://doi.org/10.1002/fld.1650200824

[17] Madenci, E., Oterkus, E., Peridynamic theory and its applications, Springer, 2014. https://doi.org/10.1007/978-1-4614-8465-3

[18] Panchadhara, R., Gordon, P. A., Application of peridynamic stress intensity factors to dynamic fracture initiation and propagation, International Journal of Fracture 201 (2016) 81–96. https://doi.org/10.1007/s10704-016-0124-8

[19] Rao, S. S., Mechanical vibrations, 5th Edition, Pearson Education, 2011.

[20] Rice, J. R., A path independent integral and the approximate analysis of strain concentration by notches and cracks, Journal of Applied Mechanics 35 (2) (1968) 379–386. https://doi.org/10.1115/1.3601206

[21] Shojaei, A., Hermann, A., Seleson, P., Silling, S. A., Rabczuk, T., Cyron, C. J., Peridynamic elastic waves in two-dimensional unbounded domains: Construction of nonlocal Dirichlet-type absorbing boundary conditions, Computer Methods in Applied Mechanics and Engineering 407 (2023) No. 115948. https://doi.org/10.1016/j.cma.2023.115948

[22] Silling, S. A., Propagation of a stress pulse in a heterogeneous elastic bar, Journal of Peridynamics and Nonlocal Modeling 3 (2021) 255–275. https://doi.org/10.1007/s42102-020-00048-5

[23] Silling, S. A., Reformulation of elasticity theory for discontinuities and long-range forces, Journal of the Mechanics and Physics of Solids 48 (1) (2000) 175–209. https://doi.org/10.1016/S0022-5096(99)00029-0

[24] Silling, S. A., Askari, E., A meshfree method based on the peridynamic model of solid mechanics, Computers & Structures 83 (17–18) (2005) 1 526–1 535. https://doi.org/10.1016/j.compstruc.2004.11.026

[25] Song, S. H., Paulino, G. H., Dynamic stress intensity factors for homogeneous and smoothly heterogeneous materials using the interaction integral method, International Journal of Solids and Structures 43 (2006) 4 830–4 866. https://doi.org/10.1016/j.ijsolstr.2005.06.102

[26] Zhu, N., Oterkus, E., Calculation of stress intensity factor using displacement extrapolation method in peridynamic framework, Journal of Mechanics 36 (2) (2020) 235–243. https://doi.org/10.1017/jmech.2019.62